

Electronic structure of zinc-blende-structure semiconductor heterostructures

Abraham Moyses Cohen*

*Departamento de Física e Ciências dos Materiais, Instituto de Física e Química de São Carlos,
13 560 São Carlos, São Paulo, Brazil*

Gilmar Eugenio Marques

Departamento de Física, Universidade Federal de São Carlos, 13 560 São Carlos, São Paulo, Brazil
(Received 3 January 1989; revised manuscript received 15 January 1990)

We present an extended $\mathbf{k}\cdot\mathbf{p}$ model to calculate the electronic structure of any direct-band-gap semiconductor heterostructure with either normal or with inverted bulk band structure. The full Hamiltonian is block diagonalized in sets of time-reversed states by an appropriated unitary transformation which separates the degenerate spin states into two blocks. The model takes into account the full degeneracy of the eight lowest Bloch states at the Γ point, the subband mixing and coupling, the warping, and the derived boundary conditions at the interface. The anisotropy is treated in perturbation theory. Subbands in quantum wells of $\text{Ga}_{1-x}\text{Al}_x\text{As}/\text{GaAs}$, of semimagnetic $\text{Cd}_{1-x}\text{Mn}_x\text{Te}/\text{CdTe}$, and of narrow-band-gap lattice-matched $\text{Ga}_{0.47}\text{In}_{0.53}\text{As}/\text{Al}_{0.48}\text{In}_{0.52}\text{As}$ are calculated as a function of the dimension and composition of the heterostructure. These examples show the effect of conduction-band–valence-band coupling, subband mixing, and the inclusion of the split-off band in the energy dispersions. Extensive comparison with experimental data and other theoretical approaches is presented.

I. INTRODUCTION

In recent years, the increasing ability to control the epitaxial growth of semiconductor crystals has made possible the fabrication of high-quality artificial heterostructures of many different geometries, doping profiles, and semiconductor classes. The III-V compound heterostructures, grown by molecular-beam epitaxy or metal-organic chemical-vapor deposition, are used in a variety of optoelectronic and electronic devices, with $(\text{Ga,Al})\text{As}/\text{GaAs}$ being the most well-known system. The magneto-optic properties of these heterolayered systems are very intriguing and have been extensively studied in the literature.^{1–3} More recently, other compounds such as $\text{Ga}_{1-x}\text{In}_x\text{As}/\text{Al}_{1-y}\text{In}_y\text{As}$ are receiving special attention due to their importance for telecommunication systems operating with silica optical fibers. These materials are grown on InP substrates and, therefore, present large lattice mismatch except for In contents of $x=0.53$ and $y=0.52$, the so-called lattice-matched heterostructure. Their physical properties have been broadly investigated in Refs. 4 and 5. The magneto-optical properties of II-VI pseudobinary-compound diluted magnetic semiconductors (DMS's) have also been studied, such as, for example, $(\text{Cd,Mn})\text{Te}/\text{CdTe}$ in Refs. 6 and 7 and $(\text{Zn,Mn})\text{Se}/\text{ZnSe}$ in Ref. 8. These DMS systems exhibit a vast range of features new to semiconductor physics.⁹ The $3d^5$ Mn ion randomly replaces the group-II element in the fcc sublattice and their antiferromagnetic spin-spin exchange interaction leads to a magnetization of the sample. Therefore, the subband structure is strongly affected and as a direct consequence so are their optical, thermal, and transport properties.

Several calculations of the subband structures, using Kane's¹⁰ $\mathbf{k}\cdot\mathbf{p}$ model within many different approximations, are found in Refs. 11–14 for metal-oxide-

semiconductor field-effect transistor interfaces, in Refs. 15 and 16 for heterojunctions, and in Refs. 17–21 for quantum wells and superlattices.

In this paper we present an extended Kane $\mathbf{k}\cdot\mathbf{p}$ model to calculate electron and hole subbands in heterostructures as a function of the parallel momentum. The model includes all eight lowest Bloch states bordering the Γ point, and the various aspects of their mixing and coupling are discussed as examples. The model applies to any III-V compound, II-VI compound, or pseudobinary DMS alloys with normal or inverted zinc-blende-structure symmetry. We have chosen three special materials, with different band gaps and spin-orbit energies, as examples for the application of our method and also compare the subband structure and the square of the optical matrix elements from the present model with the results from the tight-binding model as well as with a different approach based on the $\mathbf{k}\cdot\mathbf{p}$ model of Ref. 20.

II. THEORY

The typical bulk energy-band structure near the fundamental band gap of a zinc-blende-structure semiconductor, with normal (or direct) and with inverted structure, is schematically illustrated in Fig. 1. The conduction-band states of normal materials transform as the s -like doubly degenerate Γ_6 representation of the T_d crystallographic point group (as most of the III-V compounds) while in inverted materials, especially II-VI compounds having Hg or Se and usually referred to as zero-band-gap semiconductors, the conduction band has the p -like symmetry of the doubly degenerate ($J=\frac{3}{2}, \pm\frac{1}{2}$) Γ_8 representation.

Let us choose to order the eight periodic Bloch functions, using the $|J, M_J\rangle$ "cubic-harmonics" notation for the angular-momentum states at the Γ point, as

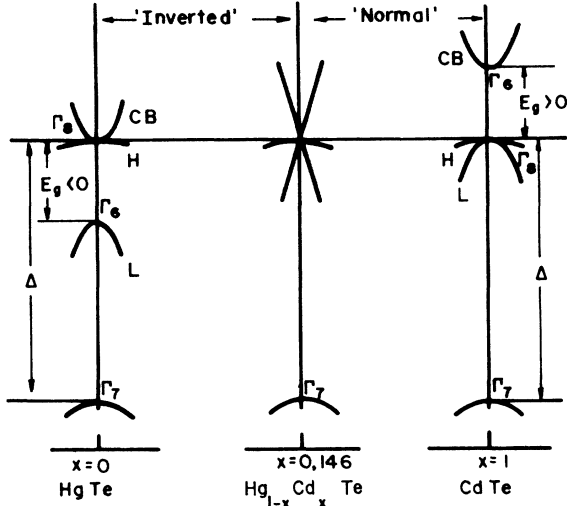


FIG. 1. Qualitative change in the bulk band structure of $\text{Hg}_{1-x}\text{Cd}_x\text{Te}$, for increasing concentration of Cd, illustrating the inverted (Hg-rich) and the normal (Cd-rich) zinc-blende-structure symmetries close to the Γ point. The inversion occurs close to Cd content $x = 0.146$.

$$\underline{H} = \begin{pmatrix} D_{el} & -\sqrt{3}A_+ & \sqrt{2}B & -B & 0 & 0 & -A_- & -\sqrt{2}A_- \\ -\sqrt{3}A_+^* & D_{hh} & \sqrt{2}L & -L & 0 & 0 & -S & -\sqrt{2}S \\ \sqrt{2}B^* & \sqrt{2}L^* & D_{lh} & Q & A_+^* & S & 0 & \sqrt{3}L \\ -B^* & -L^* & Q & D_{s.o.} & \sqrt{2}A_+^* & \sqrt{2}S & -\sqrt{3}L & 0 \\ 0 & 0 & A_+ & \sqrt{2}A_+ & D_{el} & -\sqrt{3}A_- & \sqrt{2}B & -B \\ 0 & 0 & S^* & \sqrt{2}S^* & -\sqrt{3}A_-^* & D_{hh} & \sqrt{2}L^* & -L^* \\ -A_-^* & -S^* & 0 & -\sqrt{3}L^* & \sqrt{2}B^* & \sqrt{2}L & D_{lh} & Q \\ -\sqrt{2}A_-^* & -\sqrt{2}S^* & \sqrt{3}L^* & 0 & -B^* & -L & Q & D_{s.o.} \end{pmatrix}, \quad (2)$$

where s.o. denotes spin orbit, and the matrix elements are defined in terms of combinations of the linear-momentum components, $k_x^2 + k_y^2 = k^2$, $k_{\pm} = (k_x \pm ik_y) = k \exp(\pm i\theta)$, and k_z , times Kane's parameters (atomic units), as

$$\begin{aligned} D_{el} &= E_g + E_v^c + (F + \frac{1}{2})k^2 + [\hat{k}_z(F + \frac{1}{2})\hat{k}_z], \\ D_{hh} &= D_+ \quad \text{and} \quad D_{lh} = D_- \\ D_{\pm} &= -E_v^v - \frac{1}{2}(\gamma_1 \pm \gamma_2)k^2 - \frac{1}{2}[\hat{k}_z(\gamma_1 \mp 2\gamma_2)\hat{k}_z], \\ D_{s.o.} &= -\Delta - E_v^{s.o.} - \gamma_1 k^2 - \frac{1}{2}[\hat{k}_z(\gamma_1)\hat{k}_z], \\ A_{\pm} &= \sqrt{1/6}P\hat{k}_z \pm \sqrt{2/3}\{G, \hat{k}_z\}k_{\mp}, \\ B &= \sqrt{1/3}\{P, \hat{k}_z\} - 2i\sqrt{1/3}Gk_x k_y, \\ L &= \sqrt{3/2}\{\gamma_3, \hat{k}_z\}k_-, \\ S &= \sqrt{3/2}(\bar{\gamma}k_-^2 - \mu k_+^2), \quad \bar{\gamma} = \frac{1}{2}(\gamma_2 + \gamma_3), \quad \mu = \frac{1}{2}(\gamma_3 - \gamma_2), \\ Q &= \sqrt{2}[\hat{k}_z(\gamma_2)\hat{k}_z] - \sqrt{1/2}\gamma_2 k^2. \end{aligned}$$

$$\begin{aligned} |u_1\rangle &= |\frac{1}{2}, +\frac{1}{2}\rangle = |S; \uparrow\rangle, \\ |u_2\rangle &= |\frac{3}{2}, +\frac{3}{2}\rangle = (i/\sqrt{2})|X + iY; \uparrow\rangle, \\ |u_3\rangle &= |\frac{3}{2}, +\frac{1}{2}\rangle = (i/\sqrt{6})[|X + iY; \downarrow\rangle - 2|Z; \uparrow\rangle], \\ |u_4\rangle &= |\frac{1}{2}, +\frac{1}{2}\rangle = (i/\sqrt{3})[|X + iY; \downarrow\rangle + |Z; \uparrow\rangle], \end{aligned} \quad (1a)$$

and their four twin states are

$$\begin{aligned} |u_5\rangle &= |\frac{1}{2}, -\frac{1}{2}\rangle = -|S; \downarrow\rangle, \\ |u_6\rangle &= |\frac{3}{2}, -\frac{3}{2}\rangle = -(i/\sqrt{2})|X - iY; \downarrow\rangle, \\ |u_7\rangle &= |\frac{3}{2}, -\frac{1}{2}\rangle = -(i/\sqrt{6})[|X - iY; \uparrow\rangle + 2|Z; \downarrow\rangle], \\ |u_8\rangle &= |\frac{1}{2}, -\frac{1}{2}\rangle = (i/\sqrt{3})[|X - iY; \uparrow\rangle - |Z; \downarrow\rangle]. \end{aligned} \quad (1b)$$

The set of states (1a) transforms in the set (1b), under the application of the time-reversal operator for zinc-blende-structure semiconductor symmetry, $\hat{K} = -i\sigma_y\hat{C}\hat{J}$, where σ_y is the spin Pauli matrix which flips the spin component, \hat{C} is the complex-conjugation operator, and \hat{J} is the inversion operator.

Let the z axis be perpendicular to the direction of the heterostructure. We can write an extended version of the $\mathbf{k} \cdot \mathbf{p}$ Hamiltonian in the set of Bloch states given in Eqs. (1) as

For layered systems in the flat-band condition,^{14,22} the z component of the linear momentum, perpendicular to the interface, becomes a differential operator, $\hat{k}_z = -id/dz$, whereas in the bulk it is a number.^{10,23} Also, in these expressions, $\{\hat{A}, \hat{B}\} = \frac{1}{2}(\hat{A}\hat{B} + \hat{B}\hat{A})$ is an average of the anticommutator, E_g is the smaller band gap of the materials in the heterostructure, $P(F)$ is the first-order (second-order) Kane parameter for the Γ_6 band, γ_1, γ_2 , and γ_3 are equivalent to the Luttinger parameters²⁴ for the Γ_8 band, Δ is the spin-orbit energy which splits the Γ_7 and the Γ_8 multiplets as shown in the Fig. 1, and lastly E_v^i is the band offset for the i th branch in a given interface. For bulk states the parameters $P, F, \gamma_1, \gamma_2, \gamma_3, T$, and G are independent of the coordinate z , and E_v^i is zero. Although we use the z dependence of all parameters as two different constants for each side of the heterostructure, in principle, they can change smoothly from one side of the interface to the other (graded interface). Also, we choose the zero of energy at the top of

the Γ_8 energy branch, and for this choice, the Γ_6 electrons have energies larger than E_g , the Γ_8 holes have negative energies whereas the Γ_7 split-off electrons have energies smaller than Δ . The parameter μ , in the definition of the matrix element S , gives the warping of the valence (conduction) subbands in normal (inverted) materials. The inversion asymmetry terms T for the Γ_7 and Γ_8 bands and G for the Γ_6 band are responsible for the spin splitting of the Kramers doublets in zinc-blende-structure materials. However, their values are small,²⁵⁻²⁷ and, therefore, we have chosen to treat them in perturbation theory.

We have ordered the Bloch functions at the Γ point in a convenient way for our future purpose, and it may not be the same order as used by a number of authors as for example Okhawa and Uemura,¹² Altareli, Ekenberg, and Fasolino,¹⁷ Broido and Sham,¹⁹ Eppenga, Schuurmans, and Colak,²⁰ and Liu and Sham.²⁸ However, a direct comparison becomes simple since we have listed them above.

For certain energy E , a general band structure displays solutions inside the Brillouin zone, which have real (propagating or extended Bloch functions) and complex (evanescent or localized Bloch functions) wave vectors. The complex wave vectors appear along the so-called real lines, and along these lines the energy is a real and monotonic function of the complex vector \mathbf{k} . For an extensive treatment of the properties of real lines in a given band structure see Ref. 29. In Ref. 20, the authors Eppenga, Schuurmans, and Colak have called them spurious solutions and, in their $\mathbf{k}\cdot\mathbf{p}$ method, followed an approach which avoid them by decomposing the 8×8 model for the electron-hole system into a 2×2 matrix for the electrons and a 6×6 matrix for the holes. A block decomposition becomes necessary once general solutions with the full 8×8 matrix exhibit numerical difficulties if one is interested in the total wave function as for example in the calculation of optical absorption. However, their decomposition procedure has to handle a term proportional to

$$\frac{E_g}{[E_g - E - \hbar^2(k_x^2 + k_y^2 + k_z^2)/2m_0]}$$

which, in layered systems, becomes much too complicated since k_z is a differential operator. By setting this term to $E_g/(E_g - E)$, they have avoided their spurious solutions; however, this procedure, only justified for wide-band-gap semiconductors, would lead to uncontrolled difficulties in narrow-band-gap and zero-band-gap layered systems, as for example InSb and (Hg,Cd)Te, respectively, where the role of the evanescent states is essential.³⁰ Moreover, the effect of such a procedure on the boundary conditions at a given heterointerface is not clear.

We have chosen a different approach. Since the asymmetry terms T and G are small, at first we neglected them, and therefore were able to find an unitary transformation U which block diagonalizes the 8×8 Hamiltonian into two 4×4 sets of states which are time-reversal transformations of each other. A similar procedure was done by Marques, White, and Sham^{14,30} for the 6×6 Kane Hamiltonian and by Broido and Sham¹⁹ for the 4×4 Luttinger Hamiltonian. The block-diagonalized Hamiltonian

is thus much simpler to deal with since the whole set of degenerate spin states can be treated separately without any need to impose drastic approximations. Therefore, our procedure can be applied to all different classes of material previously mentioned. Moreover, even for degenerate branches, the selection and identification of eigenvectors for the optical-absorption calculation is extremely simple and only demands a modest computational effort. After solving the full subband structure for the block-diagonalized Hamiltonian, we then include the small effect of the asymmetry and warping terms T and G in first-order perturbation theory.

In order to perform the block diagonalization, we write the Hamiltonian previously mentioned as a sum of 8×8 matrices, $\underline{H} = \underline{H}_s(\vec{\gamma}) + \underline{H}_w(\mu) + \underline{H}_a(T, G)$. Then, it is always possible to find four parameters δ , Φ , η , and ζ such that the symmetric part $\underline{H}_s(\vec{\gamma})$ transforms into two 4×4 block-diagonalized matrices under the application of the 8×8 unitary matrix

$$\hat{U} = \frac{1}{\sqrt{2}} \begin{bmatrix} \underline{R} & \underline{R} \\ -\underline{R}^* & \underline{R}^* \end{bmatrix}, \quad (3)$$

where \underline{R} is a 4×4 diagonal matrix with elements $\exp(-i\delta)$, $\exp(-i\Phi)$, $\exp(-i\eta)$, and $\exp(-i\zeta)$. The same unitary transformation on the warping part of the Hamiltonian is given by $\hat{U}^\dagger \underline{H}_w(\mu) \hat{U} = \underline{H}_{w1}(\mu) + \underline{H}_{w2}(\mu)$. Here the term \underline{H}_{w1} is block diagonalized and gives almost all the warping effect on the subband dispersions. The term \underline{H}_{w2} is not block diagonalized: its contribution to the warping is very small and only appears at large values of the parallel momentum \mathbf{k} . We have checked its effect by diagonalizing both the full 8×8 and the 4×4 matrices. Therefore, we treat the asymmetry term in $\underline{H}_a(T, G)$ as a perturbation to the states determined by the block-diagonalized Hamiltonian. In view of the great simplicity of treatment determined by this procedure, we prefer to consider the nondiagonalized part as perturbation instead of having to take a not well-controlled approximation. Also, all types of solutions are fully kept within our procedure.

After adding every blocked part of the transformed Hamiltonians, we obtain a 4×4 upper block, that we will call the U states, as

$$\underline{H}_U = \begin{bmatrix} D_{el} & P_1 & P_2 & P_3 \\ P_1^* & D_{hh} & L_1 & L_2 \\ P_2^* & L_1^* & D_{lh} & Q_1^* \\ P_3^* & L_2^* & Q_1^* & D_{s.o.} \end{bmatrix}, \quad (4)$$

where the matrix elements are defined as

$$P_1 = -\sqrt{\frac{1}{2}}Pk,$$

$$P_2 = \sqrt{\frac{2}{3}}\{P, \hat{k}_z\} + i\sqrt{\frac{1}{6}}Pk,$$

$$P_3 = -\sqrt{\frac{1}{3}}\{P, \hat{k}_z\} + i\sqrt{\frac{1}{3}}Pk,$$

$$L_1 = \sqrt{3}k\{\gamma_3, \hat{k}_z\} + i(\sqrt{3})/2k^2\gamma(\theta),$$

$$L_2 = -\sqrt{\frac{3}{2}}k\{\gamma_3, \hat{k}_z\} + i(\sqrt{\frac{3}{2}})k^2\gamma(\theta),$$

$$Q_1 = \sqrt{2}[\hat{k}_z(\gamma_2)\hat{k}_z] - \sqrt{\frac{1}{2}}\gamma_2k^2 - i(3/\sqrt{2})k\{\gamma_3, \hat{k}_z\}.$$

The diagonal operators in Eq. (4) have already been defined, and the strongest contribution to the warping of the subband structure comes from the terms proportional to $\gamma(\theta) = \gamma_3 - 2\mu \cos^2(2\theta)$. Notice that this is a two-dimensional version of the quasigermanium model for layered systems.

The lower block, for L states, satisfies the following relation, $\underline{H}_L = \underline{H}_U^*$, as required by time reversal.

In the $\mathbf{k}\cdot\mathbf{p}$ approach there are seven bulk band-structure parameters E_g , P , F , Δ , γ_1 , γ_2 , and γ_3 which are usually obtained from the fitting of the magneto-optical absorption spectra. The literature registers a large number of parameters for a given material which, in general, depends upon the approximation, on the sample, or even on the physical property fitted, and, in almost all tables of parameters, the second-order contribution to the Γ_6 effective mass, F , has been neglected. Since the fundamental band gap E_g and the spin-orbit energy Δ can be determined independently as a function of the concentration and temperature, we therefore use them to calculate the other five parameters from the measured effective masses namely, m_c^* , m_{hh}^* , m_{lh}^* , $m_{s.o.}^*$ in the [100] direction and from m_{hh}^* in the [111] direction

The eigenvalues of our blocked Hamiltonian for the bulk case (\hat{k}_z is just a number and $E_v = 0$), calculated up to second order in the components of the momentum \mathbf{k} , can be used to determine the effective mass of each kind of particle in the vicinity of the Γ point. We get for the Γ_6 effective mass (as in the original Kane's model),

$$\frac{1}{m_c^*} = 1 + 2F + \frac{4P^2}{3E_g} \left[1 + \frac{E_g}{2(E_g + \Delta)} \right], \quad (5)$$

which explicitly shows the dependence of finite spin-orbit energy of the split-off band (the warping gives no contribution here). Also, the heavy-hole effective mass in the [100] direction is determined only by the parameters γ_1, γ_2 as

$$\frac{1}{m_{hh}^*} = (\gamma_1 - 2\gamma_2), \quad (6)$$

whereas in the same direction the light-hole effective mass is coupled to the Γ_6 band as

$$\frac{1}{m_{lh}^*} = (\gamma_1 + 2\gamma_2) + \left[\frac{4P^2}{3E_g} \right]. \quad (7)$$

On the other hand, the heavy-hole effective mass in the [111] direction depends on γ_1 and γ_3 and is given by

$$\frac{1}{m_{hh}^*} = (\gamma_1 - 2\gamma_3). \quad (8)$$

Finally, the effective mass of the split-off branch is given by

$$\frac{1}{m_{s.o.}^*} = \gamma_1 + \frac{2P^2}{3E_g} \left[\frac{E_g}{(E_g + \Delta)} \right]. \quad (9)$$

Although all five parameters F , P , γ_1 , γ_2 , and γ_3 are

determined in a consistent way, the experimental values of all masses for a given material are sometimes difficult to find. It should be noticed from Eqs. (5), (7), and (9) that in the $\mathbf{k}\cdot\mathbf{p}$ model the heavy-hole branches are weakly coupled to the other valence branches in the vicinity of the Γ point. However, both light-hole and split-off branches are coupled to the conduction branch. Also, Eqs. (5), (7), and (9) clearly show how the finite spin-orbit energy influences the amount of band mixing in the valence band and coupling of the conduction band.

For a general direction $\hat{\mathbf{k}} = (\hat{k}_x, \hat{k}_y, \hat{k}_z)$ in the bulk, there is a dependence of the heavy (-) and light (+) masses on the warping, and they are given by

$$\begin{aligned} \frac{1}{m(\hat{\mathbf{k}})} = & \gamma_{1L} \mp [(\epsilon_1^2 + 3\epsilon_2^2)\gamma_{2L}^2 \\ & + 12(\hat{k}_x^2 \hat{k}_y^2 + \hat{k}_y^2 \hat{k}_z^2 + \hat{k}_z^2 \hat{k}_x^2)\gamma_{3L}^2 \\ & - 3\gamma_\mu^2 \epsilon^2]^{1/2}, \quad (10) \end{aligned}$$

where $\epsilon = (\hat{k}_x^2 + \hat{k}_y^2)$, $\epsilon_1 = (2\hat{k}_z^2 - \epsilon)$, and $\epsilon_2 = (\hat{k}_x^2 - \hat{k}_y^2)$. Also γ_{iL} are the usual parameters for the 4×4 Luttinger²⁴ Hamiltonian and $\gamma_\mu = \mu \sin(4\theta)$ measures the difference between the inclusion of the effect of warping in our block-diagonalization procedure from the solution of the 8×8 Hamiltonian.

With this set of parameters, determined uniquely for a given material, the motion of electrons and holes in the heterostructure is found from the solutions of the Schrödinger equation for each four-component spinor in the upper (U states) and in the lower (L states) blocks. Therefore, we must solve, $(H_{U(L)} + V)\Psi_{U(L)} = E_{U(L)}\Psi_{U(L)}$, where the blocked Hamiltonian is given in Eq. (4), V is a 4×4 matrix containing any external potential applied across the junction as well as the internal strains due to lattice mismatch (after appropriated unitary transformation with U). Note that the band offset, E_v , is already included in Eq. (2), and we either take their experimental and theoretical values or use it as a free parameter if its value is not known.

Let the envelope wave function for each four-component spinor be written as

$$\Psi_U(x, y, z, \mathbf{k}) = \begin{pmatrix} A_1(x, y, z, \mathbf{k}) \\ A_2(x, y, z, \mathbf{k}) \\ A_3(x, y, z, \mathbf{k}) \\ A_4(x, y, z, \mathbf{k}) \end{pmatrix} \quad (11a)$$

and

$$\Psi_L(x, y, z, \mathbf{k}) = \begin{pmatrix} A_5(x, y, z, \mathbf{k}) \\ A_6(x, y, z, \mathbf{k}) \\ A_7(x, y, z, \mathbf{k}) \\ A_8(x, y, z, \mathbf{k}) \end{pmatrix}. \quad (11b)$$

Since present heterojunctions, grown by epitaxial techniques, have interfaces of high quality, the translational invariance along the x - y plane can be assumed without a loss of reality, therefore, the explicit dependence of any component in Eqs. (11) on the parallel momentum can be separated as a plane wave in the x - y plane and a implicit dependence of the component, as

$$A_j(x, y, z, \mathbf{k}) = e^{i\mathbf{k}\cdot\mathbf{r}} A_j(z, k), \quad (12)$$

where \mathbf{k} and \mathbf{r} are two-dimensional vectors in the x - y plane and $j = 1, 2, \dots, 8$.

In the $\mathbf{k}\cdot\mathbf{p}$ method, the derivation of boundary conditions at a given interface between two different materials is fundamentally based on three assumptions.³⁰ (i) The set of Bloch functions at the Γ point is the same for both semiconductors. (ii) The interface is an ideal geometrical plane separating two thin regions of each material. (iii) Within this thin slice of the interface, the evanescent waves are indispensable to assure a smooth continuity of both the wave function as well as its normal derivative. Assumption (iii) is easily met within our procedure, and (ii) depends on the quality of real interfaces. The assumption (i) is the strongest one and deserves further discussion. Later on we will compare the results from our $\mathbf{k}\cdot\mathbf{p}$ model with the ones obtained from the tight-binding method where assumption (i) is completely relaxed.

The generalized boundary conditions at a given interface is a consequence of the flux conservation and can be easily obtained from the integration of Eq. (4) over the thin slice of the junction^{17,18,31,32} In the limit where the thickness of the slice of the interface goes to zero, the evanescent waves of each side die out, and their role become unimportant.³⁰ Therefore, the smooth matching at the interface in the position z_i is guaranteed for U states if the following operator is continuous:

$$\begin{pmatrix} F_1 & 0 & -\sqrt{2}G_2 & G_2 \\ 0 & G_- & -\sqrt{2}K_1 & K_1 \\ -\sqrt{2}G_2 & -\sqrt{2}K_1 & G_+ & Q_z^+ \\ G_2 & K_1 & Q_z^- & G_1 \end{pmatrix}, \quad (13)$$

where the matrix elements are defined by $F_1 = (F + \frac{1}{2})d/dz$, $G_{\pm} = -\frac{1}{2}(\gamma_1 \pm 2\gamma_2)d/dz$, $G_1 = -(\frac{1}{2}\gamma_1)d/dz$, $G_2 = -i\sqrt{1/12}P$, $K_1 = -i\sqrt{3/8}\gamma_3k$, and $Q_z^{\pm} = \sqrt{2}\gamma_2(d/dz) \pm i\sqrt{3}k$.

For L states, the time-reversed of the operator in the Eq. (13) must be conserved. Notice that, in the parabolic effective-mass limit, where both the interband coupling and the band mixing are neglected, the operator in Eq. (13) reduces to the well-known BenDaniel-Duke boundary conditions for each wave-function component corresponding to the four kinds of particles described by the differential operators D_{el} , D_{hh} , D_{lh} , and $D_{s.o.}$, respectively. If only the conduction-band-valence-band coupling is neglected, i.e., P is set to zero, the operator in Eq. (13) reduces to the boundary conditions used by Altarelli¹⁷ *et al.* and by Liu and Sham²⁸ for the Luttinger Hamiltonian. As a last observation, notice that in the deriva-

tion of boundary conditions in Eq. (13) we only neglected a small contribution due to warping of the Γ_8 band contained in the \underline{H}_{w_2} and the contribution from the small asymmetry terms $\underline{H}_a(T, G)$.

In the following sections we will discuss the main features of the subband structure of quantum wells for three different materials in order to explore our model, point out the effect of coupling and mixing on the subband dispersions, and compare them with experiments.

III. SUBBAND STRUCTURE OF ZINC-BLENDE-STRUCTURE HETEROSTRUCTURES

A. $\text{Ga}_{1-x}\text{Al}_x\text{As}/\text{GaAs}$

The lattice mismatch in GaAs/(Ga,Al)As heterostructures is small, thus, the particles will be mainly confined to the GaAs layer, therefore, any net strain existing in the interface can be neglected, and we may set $V=0$ in Eq. (10). Also, the best accepted³³ band offset for this heterojunction, 40–60% will be used in the following calculations unless another value is explicitly mentioned. The fundamental band gap for a given concentration x of Al is calculated from³⁴

$$E_g(x) = 1519 + 1040x + 470x^2 \text{ meV}, \quad (14)$$

and all parameters in Hamiltonians shown in Eqs. (2) and (4) are determined from the effective masses given in Table I in the text.

In Fig. 2 we present the calculated subband structure for electrons and holes in a 100-Å quantum well, as a function of the parallel momentum, for [100] and [110] directions in the x - y plane. Note that the Kramers-doublets are degenerate since the potential has inversion symmetry, and we have neglected terms depending on T and G . The valence-subband structure shows strong admixture at small values of k , represented by the anticrossing regions. This band mixing is different for each branch and comes, mainly, from the term proportional to $\gamma(\theta)$ in Eq. (4). At large values of k , the quadratic terms in the diagonal will become dominant, and, therefore, the dispersions will approach the parabolic curvatures of bulk materials.

The conduction-subband structure shows the strong nonparabolicity and subband mixing at large values of k_{\parallel} . These effects are partially due to the coupling to light holes, the split-off branches in the valence band, the wave-function penetration into the confining potential barriers, and the boundary conditions at the interfaces. The minigaps decreases rapidly with increasing subband index.

TABLE I. The full set of parameters for GaAs (1) and AlAs(2). For the alloy we use linear interpolation. The effective masses, in units of free-electron mass, are taken from Refs. 20, 34, and 35.

	$m_c^*[001]$	$m_{hh}^*[001]$	$m_{lh}^*[001]$	$m_{hh}^*[111]$	$m_{s.o.}^*[001]$	Δ (meV)
(1)	0.0665	0.3800	0.0870	0.9524	0.1735	340
(2)	0.1500	0.4785	0.2079	1.1490	0.3147	280

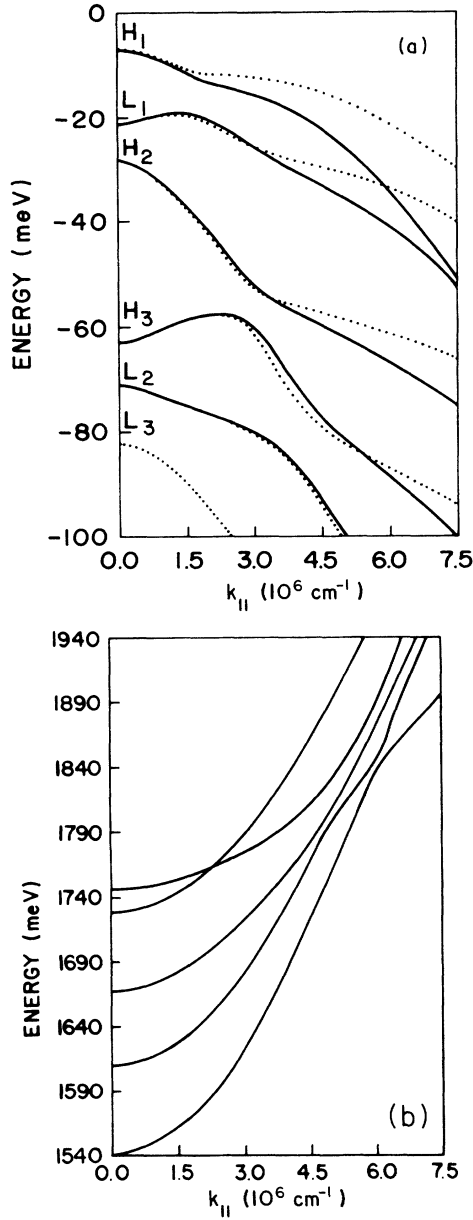


FIG. 2. The (a) valence and the (b) conduction subband structures of a 100-Å QW of $\text{Ga}_{0.70}\text{Al}_{0.30}\text{As}/\text{GaAs}$. The sequence of valence subbands, labeled as H_1 , L_1 , H_2 , L_2 , etc., indicate the origin and dominant character of each state at $k=0$. The solid lines are dispersions in the [100] direction and the dotted lines are dispersions in the [110] direction.

The importance of including the spin-orbit energy branch is shown in Fig. 3. First notice that the energy of the heavy-hole branches at $k=0$ are not affected (they are decoupled from other branches) by finite spin-orbit energy, but the light-hole branches are pulled up. As a result of this stronger mixing, the minigaps between a light-hole and a heavy-hole branch decrease whereas between two neighboring heavy-hole branches they increase. Second, the curvatures of all branches are affected by the mixing between a Γ_7 and a Γ_8 state, and, as a consequence, they will present effective masses different from their bulk values.

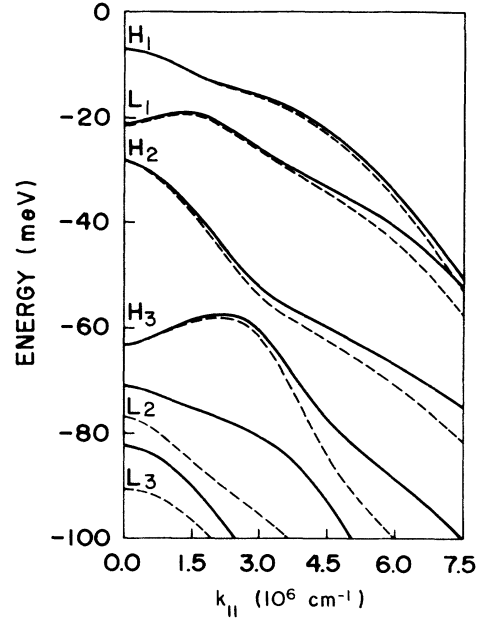


FIG. 3. Valence-subband structure of a 100-Å QW of $\text{Ga}_{0.70}\text{Al}_{0.30}\text{As}/\text{GaAs}$, along the [100] direction, calculated with finite (solid lines) and infinite (dashed lines) spin-orbit energy.

As an illustration of the effect of subband mixing and warping in different approximations, in Table II we show the values of the effective masses calculated for each species. Notice that these masses are strongly dependent on the Hamiltonian model (6×6 or 8×8) because the valence-subband mixing and the conduction-band-valence-band coupling depend on the value of the spin-orbit energy Δ . They are also affected by the band offset, by the direction of growth, and by the well width. It is clear that, due to the s character of the bottom of the conduction band, the effective mass in the quantum well (QW) as well as in the bulk does not show any angular dependence. The value for the heavy-hole mass is in excellent agreement with that reported by Duggan,³⁶ $m_{\text{hh}}^* = 0.18m_0$, for the best fit of the exciton binding energy in $(\text{Ga},\text{Al})\text{As}/\text{GaAs}$ quantum wells. Other effects of the effective masses as well as of the exciton binding energies will be discussed in the next section.

The effect of increasing the confinement can be seen in Fig. 4, where we show the valence-subband structure for a 70-Å quantum well of $\text{Ga}_{0.70}\text{Al}_{0.30}\text{As}/\text{GaAs}$. Notice

TABLE II. Effective masses, determined from quantum-well dispersions of subbands in $\text{Ga}_{0.70}\text{Al}_{0.30}\text{As}/\text{GaAs}$ with $L_z = 100$ Å, calculated with finite (F) and infinite (I) spin-orbit coupling. The light-hole masses are calculated in (a) $k=0$ and (b) off center at the maximum of the L_1 branch.

L_1 branch		k direction		
		[100] (F)	[100] (I)	[110] (F)
Electron		0.0698	0.0743	0.0698
Heavy hole		-0.1692	-0.1609	-0.1692
Light hole	(a)	0.1895	0.0969	0.1896
	(b)	-0.1785	-0.1309	-0.1543
Split off		-0.1614		-0.1616

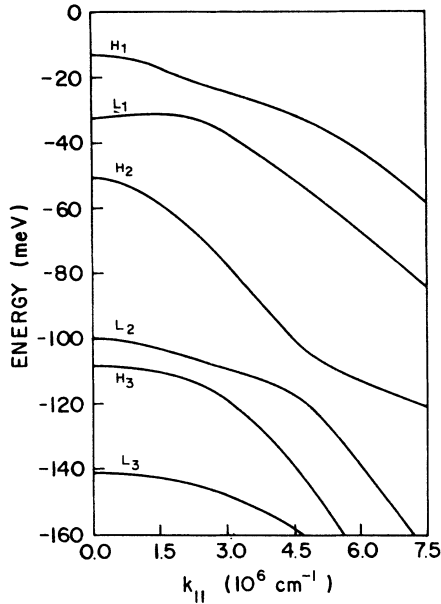


FIG. 4. Valence subband structure of a 70-Å QW of $\text{Ga}_{0.70}\text{Al}_{0.30}\text{As}/\text{GaAs}$, along the [100] direction, calculated with finite spin-orbit energy.

that, as the well width increases from 70 to 100 Å, the levels show a piling up, and this leads to an enhancement of the valence-band mixing and a change in the minigaps. The region where the effect of the diagonal quadratic terms overcome the k -linear ones also depends on the well width.

The effect of the inclusion of the split-off branch on the optical properties of quantum wells will be discussed later.

B. $\text{Cd}_{1-x}\text{Mn}_x\text{Te}/\text{CdTe}$

This material has normal zinc-blende band structure for Mn concentration⁹ below $x_m=0.7$. Above x_m the crystal structure starts to show poor quality and large (MnTe_n) islands having the wurtzite symmetry. For values of x , $0 \leq x \leq x_m$, the substitution of Cd by Mn increases the fundamental band gap and (Cd,Mn)Te acts as barrier in the heterostructure. In this sense the Mn has a similar effect as Al in (Ga,Al)As system, however the quantum well here has a much larger spin-orbit energy. The ions of Mn^{2+} are randomly distributed in the fcc sublattice of the element of group II and their half-filled $3d^5$ atomic shell are highly localized at each replaced Bravais site. The five paired spins form a local magnetic moment which displays an antiferromagnetic coupling with next neighbors. Due to thermal agitation,

(Cd,Mn)Te is paramagnetic above a certain temperature $T_g(x)$, the spin-glass freezing temperature, which depends on the Mn concentration, on the host II-VI material,³⁷ and, for heterostructures, the spin-glass phase may be totally suppressed⁷ below approximately 20 Å of layer thickness. Under no applied magnetic field, the sample magnetization is zero and the parameters for the band structure other than the band gap E_g and the band offset E_v are only slightly affected³⁸ by the concentration of Mn. The situation with an applied magnetic field is rather different and will be considered in a future publication.

The value of the band gap E_g as a function of the Mn concentration³⁹ is given by

$$E_g = 1595 + 1592x, \text{ meV} . \quad (15)$$

Since MnTe has wurtzite symmetry, the band parameters for (Cd,Mn)Te are not easy to find. We have chosen to procure all five masses at a given concentration where the alloy displays zinc-blende-structure symmetry, and for $x \leq x_m$, use linear interpolation or extrapolation to calculate the other parameters, which are given in Table III. However, this set of numbers is certainly subjected to changes once new experimental findings on its band structure are reported. It is clear, however, that this material is rather different (wide-band-gap and large-spin-orbit energy) from the previous system (large-band-gap and small-spin-orbit energy), and therefore, is a suitable example where one can check the effect of valence-band mixing and decreasing coupling to the conduction band.

The lattice mismatch in the heterostructure induces a strain in the CdTe layer,⁴⁰ therefore, the potential V , in Eq. (12), should play a role. We will not discuss this effect here, since another important parameter in the method, E_v , is not precisely known for this heterojunction. It is accepted, however, that a small fraction on the band-gap difference can be accommodated in the valence band.^{6,38} Since this point is still open for the system we have chosen to use the rule 20%(VB)-80%(CB) to determine each band offset in the present calculations.

In Fig. 5 the valence-subband structure for a 100-Å quantum well with $\text{Cd}_{0.9}\text{Mn}_{0.1}\text{Te}/\text{CdTe}$ is shown. As expected, there is very little band admixture in the dispersions since we are dealing with a material having wide-band-gap and large-spin-orbit energies. Also, due to fact that the heavy-hole masses are almost three times heavier than in the GaAs case, the band offset is smaller and the spin-orbit energy considerably larger; thus, the number of light-hole states inside the well is very small. Since, as we have shown in the previous system, the heavy holes are only weakly coupled, therefore, the mixing only appears at very small values of k_{\parallel} . This large-spin-orbit system confirms the conclusions reached in the Fig. 3, that is, an

TABLE III. The full set of parameters for (1) CdTe and (2) (Cd,Mn)Te. For the alloy we use linear interpolation. The effective masses, in units of free-electron mass, are taken from Refs. 35 and 37.

	$m_c^*[\text{001}]$	$m_{hh}^*[\text{001}]$	$m_{lh}^*[\text{001}]$	$m_{hh}^*[\text{111}]$	$m_{s.o.}^*[\text{001}]$	Δ (meV)
(1)	0.0960	0.6600	0.1000	2.7000	0.2800	910
(2)	0.0960	0.3200	0.0800	0.3200	0.1500	910

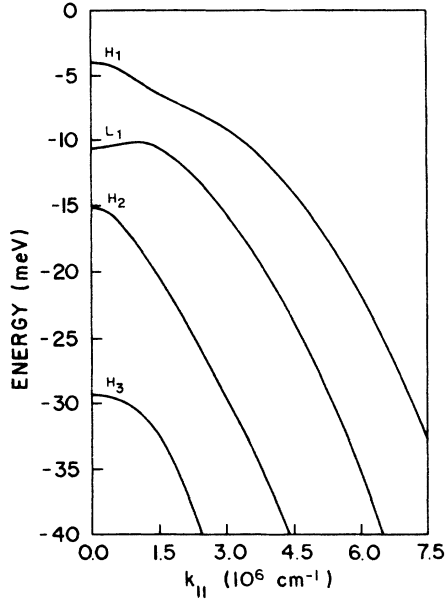


FIG. 5. Valence-subband structure of a 100-Å QW of wide-band-gap $\text{Cd}_{0.90}\text{Mn}_{0.10}\text{Te}/\text{CdTe}$, along the [100] direction, calculated with finite spin-orbit energy. The small subband mixing is mainly due to both large-spin-orbit (910 meV) and band-gap (1595 meV) energies.

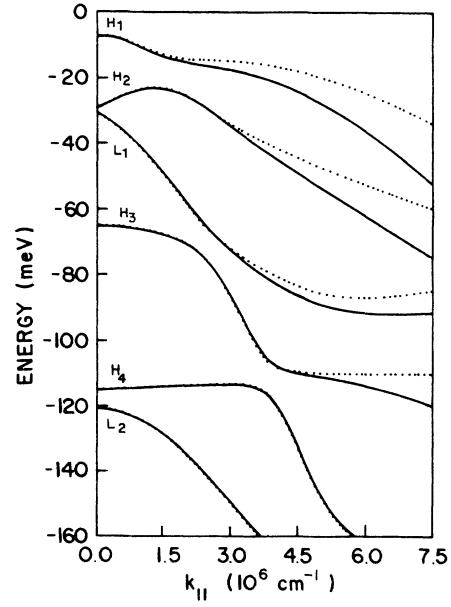


FIG. 6. Valence-subband structure of a 100-Å QW of lattice-matched (narrow-band-gap and small-spin-orbit energy) $\text{Ga}_{0.47}\text{In}_{0.53}\text{As}/\text{Ga}_{0.48}\text{In}_{0.52}\text{As}$, along the [100] direction (solid lines) and [110] direction (dotted lines). Notice the different ordering of states at $k=0$ as compared to the system described in Fig. 2.

increase in the spin-orbit energy causes a decrease in the subband mixing. Thus, away from $k=0$, the diagonal quadratic terms overcome the others, then both valence and conduction subbands resemble parabolic dispersions.

C. $\text{Ga}_{0.47}\text{In}_{0.53}\text{As}/\text{Al}_{0.48}\text{In}_{0.52}\text{As}$

The lattice-matched (Ga,In)As/(Al,In)As heterostructure has technological importance for the fabrication of fiber optical devices operating with wavelengths between 1.30 and 1.55 μm . Both concentrations of In are chosen in order to match the lattice parameter of the InP substrate, and for this case the potential V can be set to zero. Also, the band offset⁴¹ for this system is estimated to be 30–70%. The other parameters are calculated from the effective masses in Table IV. Notice here that we have quantum wells where the fundamental band gap is almost one-half that of the GaAs case, but the spin-orbit energies are almost identical. Thus, one should expect an enhancement of the subband coupling and mixing.

It is shown in Fig. 6 the valence-subband structure for a 100 Å quantum well along the [100] and [110] directions. As mentioned before, one can notice a certain

enhancement of the subband mixing when compared to Fig. 2. Moreover, the ordering of states at $k=0$ is even different from the GaAs case. In any quantum well there are two kinds of particles inside the well with different masses, and certainly the first level of the heavier particle is below the first level of the lighter particle. However, the position of the excited levels of each particle will depend on the difference of masses, on the well width and on the offset. In Fig. 7 we show the position of three lowest valence subbands of this system at $k=0$ as a function of the well width. It is seen that, above 88 Å, the second heavy-hole state is positioned below the first light-hole state. The same crossing should occur for all excited states at different well widths since, in the bulk limit $L_z \rightarrow \infty$, every heavy-hole state must be located below the top of the light-hole subband. In principle, the identification of the second peak in the optical absorption of quantum wells should certainly depend on the well width. However, we will show later that the oscillator strength for forbidden transitions, $\Delta n \neq 0$, are much weaker than the oscillator strength for transitions with $\Delta n = 0$.

On the other hand, the complexity of subband disper-

TABLE IV. The full set of parameters for lattice-matched (1) (Ga,In)As and (2) (Al,In)As. Masses, in units of free-electron mass, are taken from Refs. 4, 5, 41, and 42.

	$m_c^* [001]$	$m_{hh}^* [001]$	$m_{lh}^* [001]$	$m_{hh}^* [111]$	$m_{s.o.}^* [001]$	Δ (meV)	E_g (meV)
(1)	0.0410	0.3800	0.0520	0.7500	0.1290	360	813
(2)	0.0750	0.5700	0.0950	1.0300	0.1936	332	1.508

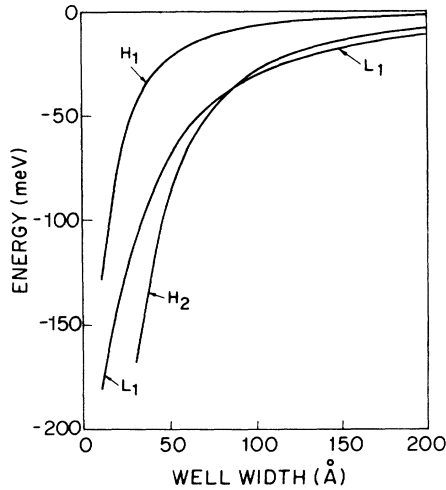


FIG. 7. The relative position of the valence-subband levels at the Γ point, for each type of particle in the lattice-matched (Ga,In)As/(Al,In)As quantum wells.

sion due to the coupling to the Γ_6 band and to the valence-band mixing will determine effective masses rather different from their bulk values. The effective mass for electrons⁵ were measured from the cyclotron-resonance experiment and from Shubnikov-de Haas experiment as well as the reduced mass⁵ for the pair electron heavy hole were measured from magnetoabsorption experiment. Their experimental values are shown in Fig. 8 together with the electronic masses determined from the dispersions of subbands for each well width. Our values are in excellent agreement with the effective masses of electrons. The experimental points for the reduced mass are above the electronic mass; however, the correct value should be below the electronic mass. We believe that these values are larger than the electronic masses because the authors in Ref. 5 have determined them through the effective

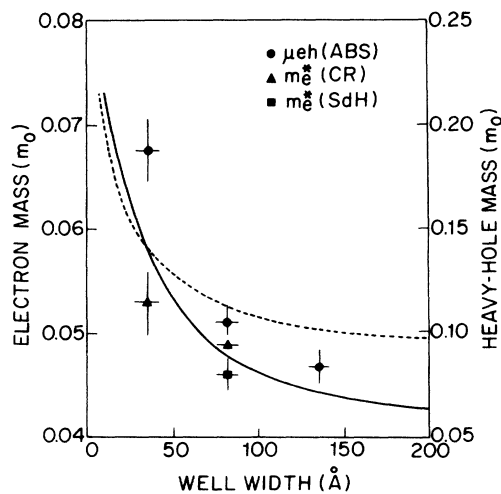


FIG. 8. The electronic (solid line) and the heavy-hole (dashed line) effective masses in lattice-matched (Ga,In)As/(Al,In)As quantum wells compared to experimental data of Ref. 4 and 5.

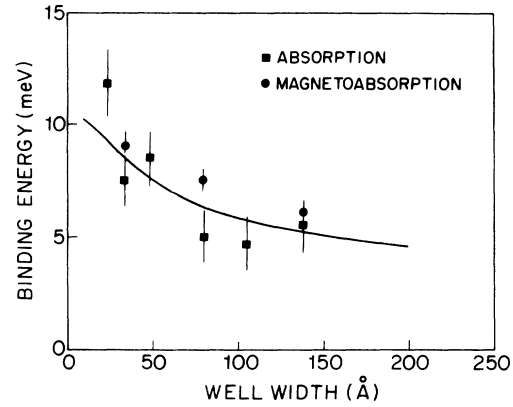


FIG. 9. The binding energy of heavy-hole excitons in the finite quantum wells, calculated with the effective masses of Fig. 8. Experimental data are taken from Ref. 4.

mass for bulk heavy holes, $m_{hh}^* = 0.066$, which is smaller than the values for the quantum wells. For further comparison, we show in Fig. 8 the effective mass for heavy holes calculated from the dispersions in the quantum wells, which takes all details of the valence-subband mixing into account. It is apparent that, for quantum wells close to 200 Å, the theoretical value of m_{hh}^* is almost the double of the bulk value used in Ref. 5. The reduced effective mass, calculated from the theoretical curves in Fig. 8, is just like the electronic curve but shifted $0.015m_0$ downwards.

In Fig. 9, we show how the binding energy of heavy-hole excitons in a finite-barrier quantum well and calculated from the effective masses of Fig. 8 compares with experimental values taken from absorption and magnetoabsorption as described in Ref. 4.

Since the position of the light holes in $k=0$ are strongly affected by the inclusion of the split-off band, therefore, it is interesting to check the spacing between the valence

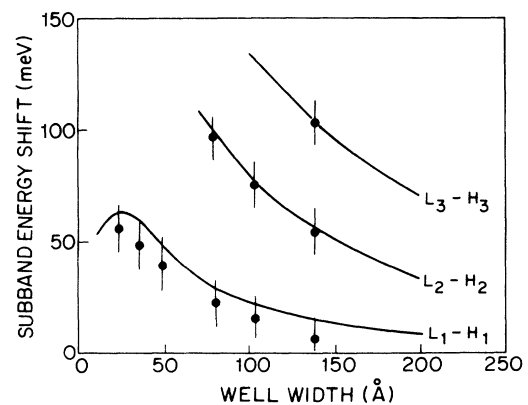


FIG. 10. The spacing between the ground states and excited states, with same quantum number, for each type of particle in the valence subbands of lattice-matched (Ga,In)As/(Al,In)As quantum wells. The experimental points are taken from Ref. 5. The difference between the binding energies of light-hole and heavy-hole excitons were included in the present calculation.

subbands through the energy difference between the transitions associated to electron heavy hole (E_m-H_n) and those associated to electron light hole (E_m-L_n). Since both the heavy-hole and light-hole excitonic effects are present in these transitions we used their binding energies, calculated as in Fig. 9, to determine these valence-subband spacings.

Figure 10 shows the energy differences for these transitions and satisfying the selection rule $n=m$, calculated with the present block-diagonalization procedure. The experimental values taken from Ref. 4 show very good agreement even for the high subband index and demonstrate how important the inclusion of the split-off band on the properties derived from the quantum-well subbands is.

Finally, we can also check the spacings between the conduction and the valence subbands. In Fig. 11 we show the comparison between the calculated energy differences, for transitions satisfying the selection rule $m=n$ and the experimental data from Ref. 4. Since the forbidden transitions are not experimentally resolved for any sample shown in Refs. 4 and 5 we will only make a comment on their effect in the optical matrix elements which will be discussed in the next section.

IV. COMPARISON TO OTHER APPROACHES

The most restrictive assumption in the $\mathbf{k}\cdot\mathbf{p}$ approach for heterostructures, namely the equality of the periodic Bloch functions at the Γ point of materials in each side, can be checked by comparing the subband structure of a given system, obtained with the $\mathbf{k}\cdot\mathbf{p}$ model and the derived boundary conditions in Eq. (13) with those obtained by the tight-binding (TB) method where such assumption

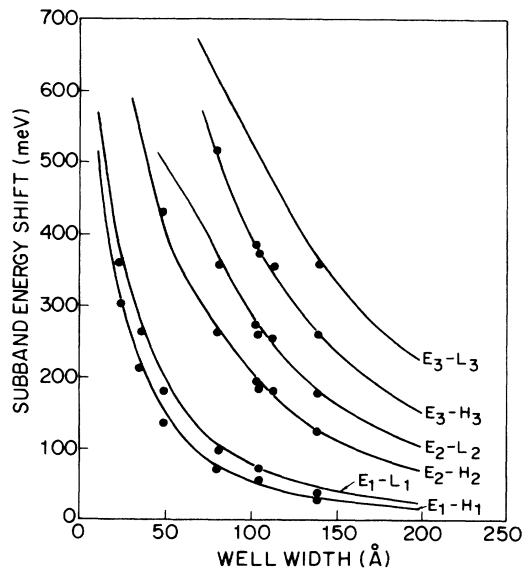


FIG. 11. The subband energy spacings ($E_m-H_m-E_g$) and ($E_m-L_m-E_g$), in lattice-matched (Ga,In)As/(Al,In)As quantum wells, calculated in the present model. The experimental data for the normally allowed optical transitions ($\Delta m = 0$) were taken from Ref. 4.

is completely relaxed. One of the most sophisticated TB model was presented by Chang and Schulman⁴³ and based on 15 optimized parameters associated with sets of atomic orbitals S , P , and S^* for each material. Also, in their TB model, the boundary conditions for the wave functions are exact in the sense that they do not depend on the kind of interface, although the choice of tight-binding matrix elements involving a function in one side with the other function in the other side of a given interface is always an approximation. The interband optical-transition probability, for a given polarization of the light ϵ , is a suitable property to check the two approaches since it depends on the full Bloch wave functions for the conduction subband $\Psi_{n,\mathbf{k}}^c(\mathbf{r})$ and for the valence subband $\Psi_{m,\mathbf{k}}^v(\mathbf{r})$ as

$$P_{m,n}(\mathbf{k}) = |\langle \Psi_{m,\mathbf{k}}^c(\mathbf{r}) | \epsilon \cdot \hat{\mathbf{P}} | \Psi_{n,\mathbf{k}}^v(\mathbf{r}) \rangle|^2, \quad (16)$$

which, due to the strong subband mixing and nonparabolicity, becomes a nontrivial function of the linear momentum \mathbf{k} along the interface. For two subbands exhibiting parabolic dispersions, $P_{n,m}$ becomes weakly dependent on $|\mathbf{k}|$, and thus the selection rules for optical transitions are strictly $m=n$. In the present system, however, the subband mixing makes transitions with $m \neq n$ (forbidden transitions) also possible, and they have been observed by Miller *et al.*⁴⁴ and by Viña *et al.*⁴⁵ The intensity of the optical transitions is determined by the oscillator strength which is, basically the average of this transition probability over the Brillouin zone.

First let us compare the subband dispersions determined by each model. Figure 12 shows the valence-subband structure for (Ga,Al)As/GaAs, calculated from

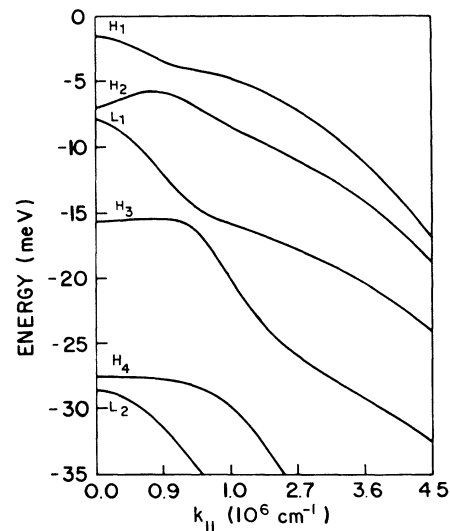


FIG. 12. Valence-subband structure of a 192 Å QW of $\text{Ga}_{0.75}\text{Al}_{0.25}\text{As}/\text{GaAs}$, along the [100] direction, calculated with 15%-85% band offset and with the same parameters used by Chang and Schulman. It is clear that there is no difference in the dispersions and in the ordering of states at $k=0$ when calculated in our block-diagonalized $\mathbf{k}\cdot\mathbf{p}$ model or in the sophisticated TB method of Refs. 43 and 44.

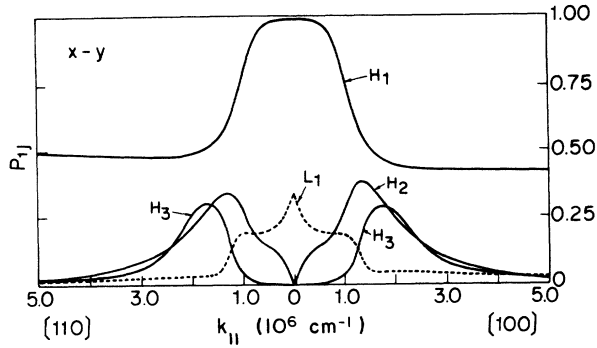


FIG. 13. The matrix elements in the x - y polarization, $P_{1,j}(\mathbf{k})$, for optical transitions from the j th valence subband to the first conduction subband, in the same quantum well described in Fig. 12. The agreement of our calculation and the optical matrix elements determined by TB model of Ref. 44 is excellent.

Eq. (4), with the same set of parameters as used by Chang and Schulman⁴³ and also by Eppenga²⁰ *et al.* assuming the old 15%-85% band offset rule. There is no difference between the subband dispersions and, particularly important for us, in the ordering of states obtained in all three methods, nevertheless the TB method was applied to a superlattice comprising 68 atomic layers ($L_z = 192 \text{ \AA}$) in the wells and 71 atomic layers ($L_B = 199 \text{ \AA}$) in the barriers. It is apparent that a superlattice with a thick barrier is definitively close to a multiple quantum well. Here, the agreement with the $\mathbf{k}\cdot\mathbf{p}$ model of Eppenga *et al.*²⁰ is certainly expected, as we mentioned before, since their procedure is only justified for large-band-gap materials such as GaAs.

The dependence of the optical probabilities $P_{m,n}(\mathbf{k})$ with the parallel momentum, in the same (Ga,Al)As/GaAs quantum well of Fig. 12, with light polarized in the x - y plane, is shown in Fig. 13. Again, one can see that they agree remarkably well with those from the $\mathbf{k}\cdot\mathbf{p}$ model of Eppenga *et al.*²⁰ and from the TB method of Schulman.⁴⁶ Therefore, it is rather clear that all three methods must present almost identical full Bloch wave functions describing the motion of particles in the heterostructure. White *et al.*³⁰ have reached similar conclusions, that is, the $\mathbf{k}\cdot\mathbf{p}$ and the TB methods, both with derived boundary conditions at the heterointerface, produce identical subband structures, Bloch wave functions and, therefore, the optical-transition probabilities. Only for light with z polarization is a small difference in the (E_1 - H_2) transition probability noticed. When calculated in the present model, $P_{12}(k=0)=0$, or in the TB model, $P_{12}(k=0)=0.02$. This small difference is due to the fact that in the TB method there is a small mixing of the light- and heavy-hole branches even at $k=0$, whereas in the $\mathbf{k}\cdot\mathbf{p}$ model the two branches are coupled only away from the zone center. However, the oscillator strengths in both methods are almost identical, and therefore, so are the calculated intensities for each optical transition.

As an example of the effect of the inclusion of the split-off subbands in the optical absorption see in Fig. 14 the transition probabilities, for an 80- \AA QW of the

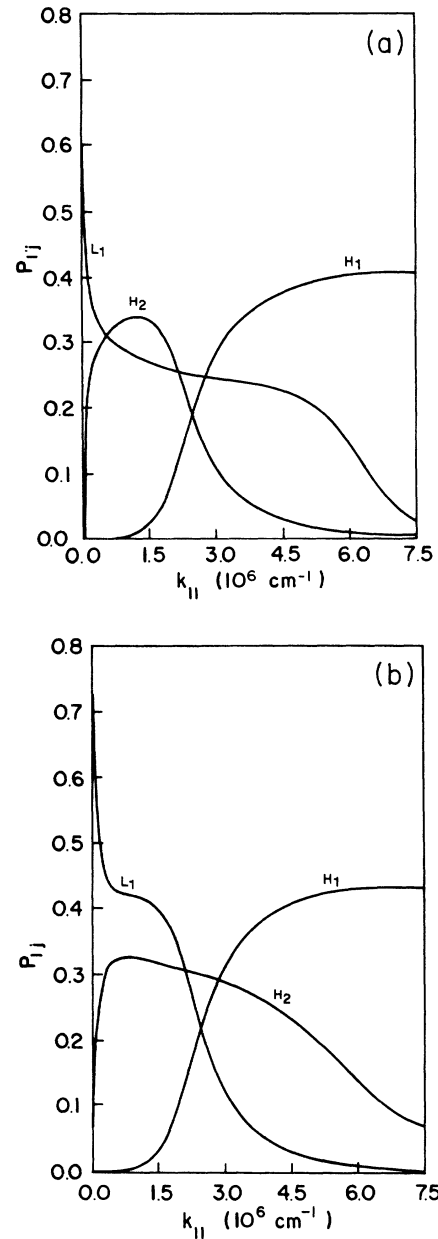


FIG. 14. The effect of the spin-orbit energy on the optical matrix elements, for z polarization and for the QW described in Fig. 7, calculated with (a) finite and (b) infinite spin-orbit energy.

narrow-band-gap and small-spin-energy-orbit (Ga,In)As/(Al,In)As, with the light polarized in the z axis, and calculated with finite [Fig. 14(a)] and with infinite [Fig. 14(b)] spin-orbit energy. In both cases the oscillator strength for the optical transition (E_1 - H_1), satisfying the rule $\Delta n = 0$, is larger than the strength for the transition (E_1 - H_2), satisfying the rule $\Delta n \neq 0$, whereas the transition (E_1 - L_1) is twice as strong as the former ones. Also, it is interesting to observe the transfer of oscillator strength from the transition (E_1 - H_2) to the transition (E_1 - L_1) as a consequence of a finite spin orbit.

On the other hand, the direction of growth has only a

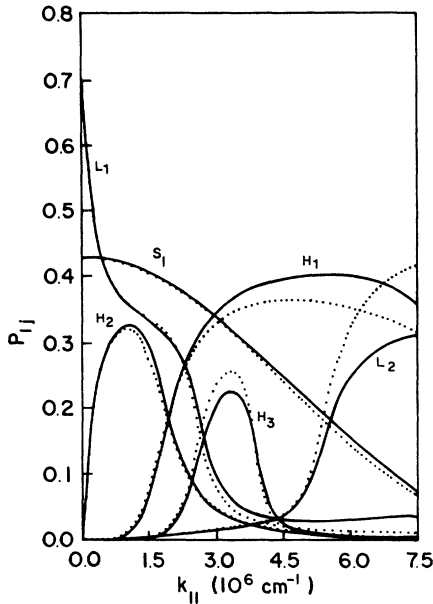


FIG. 15. The effect of the direction in the x - y plane on the optical matrix elements, for z polarization and for a QW described in Fig. 6. Solid lines in the $[100]$ direction and dotted lines in the $[110]$ direction. The matrix element, S_1 , for transition from the first split-off subband to the first conduction subband, is included.

small effect in the oscillator strength as shown in Fig. 15, where we have also included the strength S_1 for the transition (E_1 - S_1) between the first split-off state to the first conduction subband. Although this transition occurs at large values of energy ($\Delta E_{m,n} \geq 1300$ meV), its strength is comparable to (E_1 - H_3) or (E_1 - H_4), and, therefore, the identification of these peaks becomes somewhat difficult.

The last point to be addressed is how the piling up of the heavy-hole excited state below the first light-hole state, for increasing well width and shown in Fig. 7, may affect the assignment peaks in the optical spectra of quantum wells. For example, the second peak in the experimental absorption spectra of lattice-matched (Ga,In)As/(Al,In)As quantum wells above 90 Å would, in principle, be assigned to the forbidden E_1 - H_2 transition instead of the normally allowed E_1 - L_1 transition. First one must remember that forbidden optical transitions^{44,45} ($\Delta n \neq 0$) in (Ga,Al)As/GaAs quantum wells are only observed in high-quality samples and show considerably weaker strength than the normally allowed ones ($\Delta n = 0$). Second, the forbidden transitions are not resolved in any of the optical spectra reported in Refs. 4 and 5. Although the valence subbands are ordered in different sequences when calculated by the present model ($H_1, H_2, L_1, L_2, L_3, H_3, \dots$) [see Fig. 16(a)] or for infinite (6×6 model) spin orbit ($H_1, L_1, H_2, L_2, L_3, H_3, \dots$) [see Fig. 16(b)] the transition (E_2 - H_2) has a larger energy difference than the much stronger peak due to the (E_1 - L_1) transition, and therefore the second peak in the spectrum must be assigned to the light-hole one.

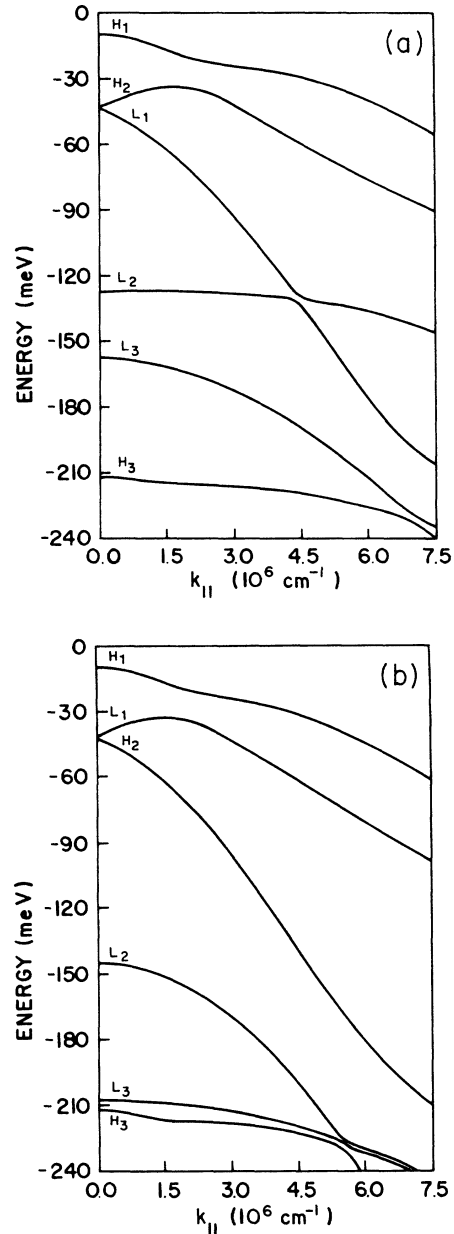


FIG. 16. Valence-subband structure of a 80-Å QW of lattice-matched (narrow-band-gap and small-spin-orbit energy) $\text{Ga}_{0.47}\text{In}_{0.53}\text{As}/\text{Ga}_{0.48}\text{In}_{0.52}\text{As}$, along the $[100]$ direction, calculated with (a) finite and (b) infinite spin-orbit energy. Notice the effect of the split-off valence band in changing the ordering of states at $k = 0$.

V. FINAL COMMENTS AND CONCLUSIONS

We have presented a general $\mathbf{k} \cdot \mathbf{p}$ method based on the 8×8 Kane type of Hamiltonian, where there exist five parameters determined from the experimental bulk effective masses for the conduction, light-hole, heavy-hole, and split-off branches of any zinc-blende-structure semiconductor with direct or inverted band structure. Our approach is based in a block-diagonalization procedure which treats the symmetry terms exactly and the asym-

metry terms in perturbation theory. Therefore, this procedure is exact for materials with diamond structure and becomes a very good approximation for zinc-blende-structure materials since they display very small values for these parameters. We have derived the boundary conditions for the envelope-function components by requiring the conservation of the current of probability across the heterointerface. In our procedure, the subband structure and optical matrix elements are in excellent agreement with the ones obtained by the sophisticated tight-binding method developed by Chang and Schulman.^{43,46} Therefore, one can assume that the Bloch wave functions in both approaches are quite similar. Thus, the boundary conditions of Eq. (13) are appropriated to describe the motion of particles in layered systems. Our method is more general and simpler than the method described in Ref. 20 since there is no approximation in our block-diagonalization procedure. Also, in the present formalism, the degenerate states are explicitly separated, and, in consequence, their numerical calculations become easier.

The overall accuracy in our method, as well as in the TB method, depend on the number of basis functions used. In the Fig. 17 we show the change in the subband structure of quantum wells for different number of functions in each kind of particle and spin component. With 15 functions our $k \cdot p$ results converge to the TB results of Chang and Schulman calculated with 20 functions. Bauer and Ando⁴⁷ have reported that, for the 4×4 Luttinger Hamiltonian, it is necessary to have 30 functions to reach virtually exact results. We have observed that, to get a good convergence for the energy values at $k = 0$ it is necessary to have only a few wave functions (approximately eight functions); however, the good description of dispersions at large values of k_{\parallel} and also at high subband index requires at least 15 functions.

Finally, special features such as a good knowledge of band offset and precise values for full bulk effective masses, band gaps, and spin-orbit energies are indispensable ingredients for an accurate description of electronic properties in the heterostructures. For some materials they are difficult to find and all reports are welcome.

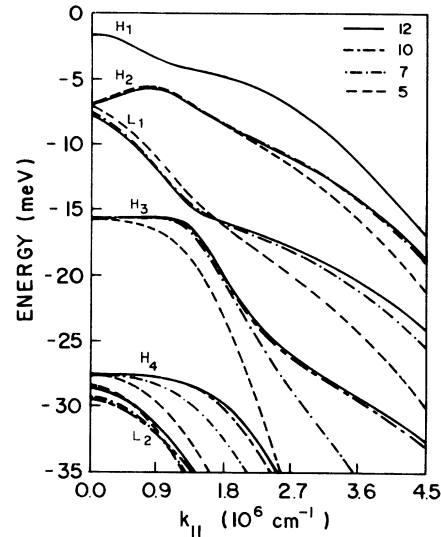


FIG. 17. The effect of the number of basis functions used to calculate the valence-subband structure of the quantum well described in Fig. 12. The dependence on the number of functions (5, 7, 10, and 12) is more pronounced at large values of k_{\parallel} and high subband indices. Above five functions, the dispersion of the H_1 subband becomes virtually exact.

ACKNOWLEDGMENTS

One of us (G.E.M.) acknowledges the partial financial support from Conselho Nacional de Desenvolvimento Científico e Tecnológico (CNPq) and the other (A.M.C.) acknowledges a leave of absence from the Departamento de Física, Universidade do Amazonas. We also are indebted to V. A. Chitta for valuable contribution. The numerical calculations were performed on the Digital Equipment Corporation VAX 11/780 computer system at the Instituto de Física e Química de São Carlos, Universidade de São Paulo.

*Permanent address: Departamento de Física, Universidade Federal do Amazonas, Caixa Postal 378, 69000, Manaus, Amazonas, Brazil.

¹D. C. Rogers, J. Singleton, R. J. Nicholas, C. T. Foxon, and K. Woodbridge, *Phys. Rev. B* **34**, 4002 (1986).

²J. C. Mann, *Surf. Sci.* **196**, 516 (1986).

³R. Bauer, D. Bimberg, Jr., Christen, D. Oertel, D. Mars, J. N. Miller, T. Fukunaga, H. Nakashima, in *Proceedings of the 18th International Conference on the Physics of Semiconductors, Stockholm, 1986*, edited by O. Engström (World Scientific, Singapore, 1987), p. 525.

⁴W. Stolz, J. C. Mann, M. Altarelli, T. Tapfer, and K. Ploog, *Phys. Rev. B* **36**, 4301 (1987).

⁵W. Stolz, J. C. Mann, M. Altarelli, T. Tapfer, and K. Ploog; *Phys. Rev. B* **36**, 4310 (1987).

⁶J. Warnock, A. Petrou, R. B. Bicknell, N. C. Giles-Taylor, D.

K. Blanck, J. F. Schetzina, *Phys. Rev. B* **32**, 6116 (1985).

⁷D. D. Awschalom, G. Grinstein, J. Yoshino, H. Munekata, and L. L. Chang, *Surf. Sci.* **196**, 649 (1988).

⁸R. L. Gunshor, L. A. Kolodziejki, N. Otsuka, S. Datta, *Surf. Sci.* **174**, 552 (1986).

⁹N. B. Brandt and V. V. Moshchalkov, *Adv. Phys.* **33**, 193 (1985).

¹⁰E. O. Kane, in *Semiconductors and Semimetals*, edited by R. K. Willardson and A. C. Beer (Academic, New York, 1966), Vol. 1, p. 75.

¹¹F. Stern, *Phys. Rev. B* **5**, 4891 (1972).

¹²F. J. Ohkawa and Y. Uemura, *J. Phys. Soc. Jpn.* **37**, 1325 (1974).

¹³G. Bastard, *Phys. Rev. B* **24**, 5693 (1981); **25**, 7584 (1982).

¹⁴G. E. Marques and L. J. Sham, *Surf. Sci.* **113**, 131 (1982).

¹⁵T. Ando, *J. Phys. Soc. Jpn.* **51**, 3893 (1982).

- ¹⁶F. Stern and S. Das Sarma, *Phys. Rev. B* **30**, 840 (1984).
- ¹⁷M. Altarelli, *Physica B+C (Amsterdam)* **117&118B**, 747 (1983); M. Altarelli, U. Ekenberg, and A. Fasolino, *Phys. Rev. B* **32**, 5138 (1985).
- ¹⁸G. Bastard and J. A. Brum, *IEEE J. Quantum Electron* **QE-22**, 1625 (1986).
- ¹⁹D. A. Broido and L. J. Sham, *Phys. Rev. B* **3**, 439 (1985).
- ²⁰R. Eppenga, M. F. H. Schuurmans, and S. Colak, *Phys. Rev. B* **36**, 1554 (1987).
- ²¹V. A. Chitta and G. E. Marques, *Semicond. Sci. Technol.* **3**, 564 (1988).
- ²²M. H. Weiler, in *Semiconductors and Semimetals*, edited by R. K. Willardson and A. C. Beer (Academic, New York 1981), Vol. 16, p. 119.
- ²³L. J. Sham and M. Nakayama, *Phys. Rev. B* **20**, 734 (1979).
- ²⁴J. M. Luttinger, *Phys. Rev.* **102**, 1030 (1956).
- ²⁵G. Dresselhaus, *Phys. Rev.* **100**, 580 (1955).
- ²⁶M. Cardona, N. E. Christensen, and G. Fasol, *Phys. Rev. Lett.* **56**, 2831 (1988).
- ²⁷M. Cardona, N. E. Christensen, and G. Fasol, *Phys. Rev. B* **38**, 1806 (1988).
- ²⁸Y. R. Lin-Liu and L. J. Sham, *Phys. Rev. B* **32**, 5561 (1985).
- ²⁹V. Heine, *Proc. Phys. Soc. London* **81**, 300 (1963).
- ³⁰S. R. White, G. E. Marques, and L. J. Sham, *J. Vac. Sci. Technol.* **21**, 544 (1982).
- ³¹D. J. BenDaniel and C. B. Duke, *Phys. Rev.* **152**, 683 (1966).
- ³²G. Bastard, *Phys. Rev. B* **24**, 5693 (1981).
- ³³J. Menendez, A. Pinczuk, D. J. Werder, A. C. Gossard, and J. H. English, *Phys. Rev.* **B33**, 8863 (1986).
- ³⁴H. C. Casey, Jr. and M. B. Panish, in *Heterostructure Lasers*, edited by Y. H. Pao and P. Kelly (Academic, New York, 1978).
- ³⁵P. Lawetz, *Phys. Rev. B* **4**, 3460 (1971).
- ³⁶G. Duggan, *Phys. Rev. B* **37**, 2759 (1988); P. Dawson, K. J. Moore, G. Duggan, H. I. Ralph, and C. T. Foxon; *ibid.* **34**, 6007 (1986).
- ³⁷D. Heiman, P. Becla, R. Kershaw, R. Ridgley, K. Dwight, A. Wold, and R. R. Galaska, *Phys. Rev. B* **34**, 3961 (1986).
- ³⁸X. C. Zang, S. K. Chang, A. V. Nurmikko, L. A. Kolodziejski, R. L. Gunshor, and S. Datta, *Phys. Rev. B* **31**, 4056 (1985).
- ³⁹Y. R. Lee and A. K. Ramdas, *Solid State Commun.* **51**, 861 (1984).
- ⁴⁰S. K. Chang, H. Nakata, A. V. Nurmikko, L. A. Kolodziejski, R. L. Gunshor, and L. A. Kolodziejski, *Appl. Phys. Lett.* **51**, 557 (1987).
- ⁴¹R. People, K. W. Wecht, K. Alavi, and A. Y. Cho, *Appl. Phys. Lett.* **43**, 118 (1983).
- ⁴²R. L. Aggarwal, in *Semiconductors and Semimetals*, edited by R. K. Willardson and A. C. Beer (Academic, New York, 1972), Vol. 9, p. 151.
- ⁴³Y. C. Chang and J. N. Schulman, *Phys. Rev. B* **31**, 2056 (1985).
- ⁴⁴R. C. Miller, D. A. Kleinman, W. A. Nordland, Jr., and A. C. Gossard, *Phys. Rev. B* **22**, 863 (1980); C. Weisbuch, R. C. Miller, R. Dingle, A. C. Gossard, and W. Wiegmann, *Solid State Commun.* **37**, 219 (1981).
- ⁴⁵L. Viña, R. T. Collins, E. E. Mendez, and W. I. Wang; *Phys. Lett.* **58**, 832 (1987).
- ⁴⁶Y. C. Chang and J. N. Schulman, *Phys. Rev. B* **31**, 2069 (1985).
- ⁴⁷G. E. W. Bauer and T. Ando, *Phys. Rev. B* **38**, 6015 (1988).